8-27-2019

Near-field Effects on Partially Coherent Light Scattered by an Aperture

Milo W. Hyde IV
Air Force Institute of Technology

Michael J. Havrilla
Air Force Institute of Technology

Recommended Citation

Hyde, M. W., & Havrilla, M. J. (2019). Near-field effects on partially coherent light scattered by an aperture. Journal of Physics Communications, 3(8), 085012. https://doi.org/10.1088/2399-6528/ab3b63

Journal of Physics Communications

OPEN ACCESS

RECEIVED
23 May 2019

ACCEPTED FOR PUBLICATION
15 August 2019

PUBLISHED
27 August 2019

PAPER

Near-field effects on partially coherent light scattered by an aperture

Milo W Hyde IV and Michael J Havrilla

Air Force Institute of Technology, 2950 Hobson Way, Dayton, OH, 45433, United States of America

E-mail: milo.hyde@us.af.mil

Keywords: coherence, diffraction, electromagnetics, method of moments, physical optics, scattering, statistical optics

Abstract

We investigate how the near field affects partially coherent light scattered from an aperture in an opaque screen. Prior work on this subject has focused on the role of surface plasmons, and how they affect spatial coherence is well documented. Here, we consider other near-field effects that might impact spatial coherence. We do this by examining the statistics of the near-zone field scattered from an aperture in a perfect electric conductor plane—a structure that does not support surface plasmons. We derive the near-field statistics (in particular, cross-spectral density functions) by applying electromagnetic equivalence theorems and the Method of Moments. We find, even in the absence of surface plasmons, that near-field physics can affect the coherence of the scattered field. The analysis and findings presented herein complement the existing coherence-related surface plasmons literature, and could find use in the design of photonic devices built to engineer spatial coherence.

1. Introduction

Motivated by the discovery of directional thermal emission (DTE), near-field effects on coherence have been studied for the past 30 years. In 1988, the first experimental results of directional emission from a heated grating were published [1, 2]. Since that time, DTE has been linked both theoretically and experimentally to the excitation of surface plasmons [3–6], and recently, fabricated structures designed to directionally emit thermal light at specific wavelengths have been demonstrated [7–10].

Directionality of a source implies spatial coherence; the existence of DTE proves that near-field physics can have a significant impact on source coherence. In the case of DTE, this impact is profound in that an initially incoherent source (a thermal source) is transformed into a partially coherent one by the excitation of surface plasmons interacting with wavelength-scale structures.

Realizing the potential of this transformation, several authors have proposed using surface plasmons and wavelength-scale structures to precisely control spatial coherence for reasons other than just spectral or directional emission [11–17]. These plasmonic methods would permit coherence manipulation at the nano- or micrometer scale—coherence control on a microchip—and be superior in terms of size, weight, power, and complexity to the more traditional approaches for coherence control [18–23]. Even at longer wavelengths, where true surface plasmons are not excited, researchers have fabricated materials to excite so-called 'spoof plasmons' [24–27]. Although these spoof plasmons have not been used to affect spatial coherence to date, in principal, they could be used for that purpose.

With the link between surface plasmons and coherence well established, we seek to answer whether there are other near-field phenomena (perhaps secondary or tertiary effects) that can impact spatial coherence. We do this by examining the scattering of a partially coherent wave from an aperture in an infinite perfect electric conductor (PEC) plane—a structure that does not support surface plasmons. We simplify the analysis and computational burden by assuming a two-dimensional (2D), z-invariant geometry; applying our results to a three-dimensional (3D) aperture geometry is straightforward.

In this paper, we derive the transverse magnetic (TM) and transverse electric (TE) expressions for the cross-spectral density (CSD) function [18, 28] in the aperture using electromagnetic (EM) theory and the commonly used physical optics (PO) approximation [29–31]. In the former case, we apply Love's equivalence theorem and

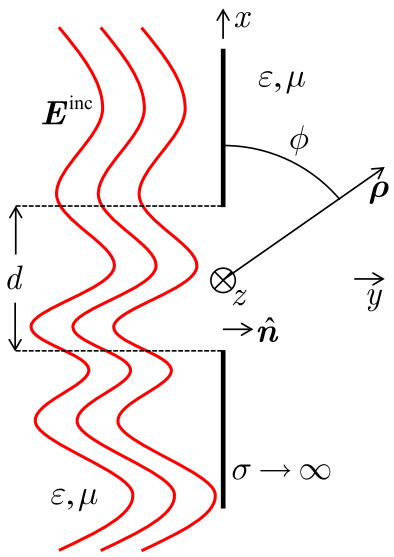

Figure 1. Aperture in a PEC ($\sigma \to \infty$) plane.

image theory [29–31], and enforce the continuity of transverse aperture fields to derive a magnetic field integral equation (MFIE) for the unknown equivalent magnetic current (proportional to the electric field in the aperture). Then, using the Method of Moments (MoM) [30, 32, 33], we numerically solve for the CSD of this current. We compare and contrast the exact EM and PO normalized CSD functions, also known as the spectral degrees of coherence (SDoCs) [18, 28], and discuss their physical significance.

We find that, even in the absence of surface plasmons, the near field does affect spatial coherence, and its impact on the far-zone intensity (or equivalently, the spectral density when working in the space-frequency domain [28]) is most pronounced at large, nonparaxial, scattering angles. We also find, even for relatively large apertures and depending on the incident field's SDoC, that near-field effects can still be observed.

The analysis and findings presented in this paper complement the existing near-field coherence research involving surface plasmons, and will be useful in future photonic devices that manipulate or control spatial coherence.

2. Analysis

2.1. Aperture geometry and assumptions

Figure 1 depicts the scattering geometry considered in this paper. A stochastic field, incident from the left, illuminates a slit of width d in an infinitesimally thin PEC ($\sigma \to \infty$) plane immersed in a linear, homogeneous, and isotropic medium with permittivity ε and permeability μ. We assume that the scatterer and the incident field are z-invariant. As a result, Maxwell's equations decouple into independent TM and TE sets, and the general 3D problem becomes 2D. We observe the resulting scattered field in the slit at $y = 0$ and in the far-zone as a function of ϕ.

We note that the incident field shown in figure 1 should be interpreted as a single realization of a whole ensemble of fields, and hence, the scattered field, resulting from that incident field, should be interpreted in the same manner. We infer physical behavior of both the incident and scattered fields from statistical moments taken over the whole ensemble of possible fields.

Since we are concerned with coherence, we require only the first and second moments of the fields, better known as the mean and CSD function, respectively. To find these moments for the scattered field, we must know the incident field's mean and CSD function. We assume that the former is zero and hence, the mean scattered field is also zero. For the latter, we assume a Schell-model [18, 28, 34] form for the incident field CSD function, and further, that the mean intensity of the incident field fully and uniformly illuminates the slit. These two assumptions result in a CSD function of the form

$$\langle E_\alpha^{\text{inc}}(x_1) E_\alpha^{\text{inc}*}(x_2)\rangle = W_{\alpha\alpha}^{\text{inc}}(x_1, x_2) = I_0 \gamma(x_1 - x_2), \tag{1}$$

where $\alpha = x, z$ for TM and TE polarizations, respectively, I_0 is the average intensity, and γ is the SDoC [18, 28, 34].

2.2. MFIEs

Returning briefly to figure 1, by applying Love's equivalence theorem and image theory [29–31], we transform the aperture geometry into an equivalent one, in which a magnetic current $\boldsymbol{\mathcal{M}}$ radiates in unbounded space. This current is unknown, and we derive an equation for $\boldsymbol{\mathcal{M}}$ in terms of the incident field by enforcing the continuity of the transverse magnetic field in the slit, namely,

$$-\hat{\boldsymbol{n}} \times \boldsymbol{H}^{\text{inc}}(x, 0) = \hat{\boldsymbol{n}} \times \frac{1}{\text{j}\omega\mu\varepsilon}(k^2 + \nabla\nabla\cdot)\boldsymbol{F}(x, 0) \quad x \in [-d/2, d/2], \tag{2}$$

where $\hat{\boldsymbol{n}}$ is the unit normal to the slit ($\hat{\boldsymbol{y}}$ here), $k = \omega\sqrt{\mu\varepsilon}$ is the wavenumber, ω is the radian frequency, and ∇ is the del operator.

The remaining symbols in equation (2) are $\boldsymbol{H}^{\text{inc}}$, which is the incident magnetic field, and $\boldsymbol{F}$, which is the electric vector potential [29, 30]. $\boldsymbol{F}$ contains $\boldsymbol{\mathcal{M}}$ and is given by the integral expression

$$\boldsymbol{F}(x, 0) = \int_{-d/2}^{d/2} \varepsilon[2\boldsymbol{\mathcal{M}}(x')]\frac{H_0^{(2)}(k|x - x'|)}{\text{j}4}\,\text{d}x'. \tag{3}$$

Note that $\boldsymbol{\mathcal{M}}$ is related to the electric field in the slit by

$$\boldsymbol{\mathcal{M}} = -\hat{\boldsymbol{n}} \times \boldsymbol{E}. \tag{4}$$

We will return to this simple relation when we present the PO solutions.

For TM polarization, $\boldsymbol{H}^{\text{inc}}$ and $\boldsymbol{\mathcal{M}}$ are z directed, and equation (2) simplifies to

$$\frac{2}{k}E_x^{\text{inc}}(x) = \int_{-d/2}^{d/2} \mathcal{M}^{\text{TM}}(x')H_0^{(2)}(k|x - x'|)\,\text{d}x'. \tag{5}$$

In the case of TE polarization, $\boldsymbol{H}^{\text{inc}}$ and $\boldsymbol{\mathcal{M}}$ are x directed, and equation (2) becomes

$$2kE_z^{\text{inc}}(x) = \left(k^2 + \frac{\partial^2}{\partial x^2}\right)\int_{-d/2}^{d/2} \mathcal{M}^{\text{TE}}(x')H_0^{(2)}(k|x - x'|)\,\text{d}x'. \tag{6}$$

Note that the condition on x specified in equation (2) applies to these equations as well. We solve these two MFIEs for their respective $\mathcal{M}$ in the next section.

2.3. MoM solutions

The first step in the MoM is to expand $\mathcal{M}$ in a set of basis functions. These basis functions should match, as closely as possible, the physical behavior of the current. After expansion, the resulting integral equation is 'tested' by taking the inner product of both sides of the equation with another set of functions known as testing functions. For accurate results, the combination of basis and testing functions must overcome the source-point singularity in the Green's function (Hankel function) and make the expressions on the right-hand sides of equations (5) and (6) integrable.

We begin with the TM polarization MFIE given in equation (5). Being in the z direction, $\mathcal{M}^{\text{TM}}$ goes like $1/\sqrt{x}$ at the slit edges [35, 36], and the Hankel function, at the source-point singularity, goes like $\ln(x)$. Taking these two factors into account, we choose rectangular basis and delta testing functions to discretize equation (5) in a procedure called point matching [30, 33, 37]. Equation (5) becomes

$$\frac{2}{k}E_x^{\text{inc}}(x_j) = \sum_i m_i^{\text{TM}} \int_{-d/2}^{d/2} \text{rect}\left(\frac{x' - x_i}{w}\right)H_0^{(2)}(k|x_j - x'|)\,\text{d}x', \tag{7}$$

where m_i^{TM} is the unknown complex weight of the ith basis function, x_i is the center of the ith rectangular basis function, w is the width of a basis function (assumed to have equal widths), x_j is the location of the jth delta testing function, and $\text{rect}(x)$ is [38]

$$\text{rect}(x) = \begin{cases} 1 & |x| < 1/2 \\ 1/2 & |x| = 1/2 \\ 0 & \text{otherwise} \end{cases}. \tag{8}$$

Note that the delta testing functions are located at the centers of the rectangular basis functions.

We now proceed to the TE polarization MFIE given in equation (6). The x-directed $\mathcal{M}^{\text{TE}}$ must go to zero at the slit edges and does so like $\sqrt{x}$ [35, 36]. Although the Hankel function at the source-point singularity behaves like $\ln(x)$, the derivatives on the outside of the integral require a higher-order combination of basis and testing functions than in the TM case to make the expression integrable.

Using the symmetry of the Green's function and some basic calculus, we redistribute one of the derivatives to operate on $\mathcal{M}^{\text{TE}}$ yielding

$$2kE_z^{\text{inc}}(x) = k^2\int_{-d/2}^{d/2}\mathcal{M}^{\text{TE}}(x')H_0^{(2)}(k|x-x'|)\,\mathrm{d}x' + \frac{\partial}{\partial x}\int_{-d/2}^{d/2}\left[\frac{\partial}{\partial x'}\mathcal{M}^{\text{TE}}(x')\right]H_0^{(2)}(k|x-x'|)\,\mathrm{d}x'. \quad (9)$$

We now choose triangular basis functions that span two discretized aperture segments, and rectangular testing functions that extend from the center of one segment to the center of an adjacent segment [33]. Note by choosing triangular basis functions, we ensure that $\mathcal{M}^{\text{TE}}$ goes to zero at the slit edges. Substituting in these functions and simplifying produces

$$\begin{aligned}
&2k\int_{-d/2}^{d/2}\text{rect}\left(\frac{x-x_j}{w}\right)E_z^{\text{inc}}(x)\mathrm{d}x\\
&=\sum_i m_i^{\text{TE}}\Bigg\{k^2\int_{-d/2}^{d/2}\text{rect}\left(\frac{x-x_j}{w}\right)\int_{-d/2}^{d/2}\Lambda\left(\frac{x'-x_i}{w}\right)H_0^{(2)}(k|x-x'|)\,\mathrm{d}x'\mathrm{d}x\\
&\quad+\frac{1}{w}\Bigg[\int_{-d/2}^{d/2}\text{rect}\left(\frac{x'-x_{i-1/2}}{w}\right)H_0^{(2)}(k|x_{j+1/2}-x'|)\,\mathrm{d}x'\\
&\quad-\int_{-d/2}^{d/2}\text{rect}\left(\frac{x'-x_{i+1/2}}{w}\right)H_0^{(2)}(k|x_{j+1/2}-x'|)\,\mathrm{d}x'\\
&\quad-\int_{-d/2}^{d/2}\text{rect}\left(\frac{x'-x_{i-1/2}}{w}\right)H_0^{(2)}(k|x_{j-1/2}-x'|)\,\mathrm{d}x'\\
&\quad+\int_{-d/2}^{d/2}\text{rect}\left(\frac{x'-x_{i+1/2}}{w}\right)H_0^{(2)}(k|x_{j-1/2}-x'|)\,\mathrm{d}x'\Bigg]\Bigg\},
\end{aligned} \quad (10)$$

where $\Lambda(x)$ is [38]

$$\Lambda(x) = \begin{cases}1-|x| & |x|\leqslant 1\\ 0 & \text{otherwise}\end{cases}. \quad (11)$$

The final form for both the TM and TE discretized MFIEs—equations (7) and (10), respectively—is

$$\boldsymbol{b} = \underline{\mathbf{Z}}\boldsymbol{m}. \quad (12)$$

Here, $\boldsymbol{b}$ is a vector containing the incident field in the aperture, $\boldsymbol{m}$ is a vector containing the unknown basis function weights and physically represents the magnetic current, and $\underline{\mathbf{Z}}$ is the impedance matrix, which physically models how the field radiated from a current element affects or couples to every other element. Since $\underline{\mathbf{Z}}$ contains all the near-zone interactions of the aperture field, it is instrumental in determining how and to what extent the near field affects spatial coherence. We will return to $\underline{\mathbf{Z}}$ in a later section.

Lastly, the far-zone electric field radiated by these currents is

$$E^{\text{MoM}}(\boldsymbol{\rho}) = \sqrt{\frac{\mathrm{j}k}{2\pi}}\frac{\exp(-\mathrm{j}k\rho)}{\sqrt{\rho}}w\begin{cases}\hat{\boldsymbol{\phi}}\ \text{sinc}\left(k\frac{w}{2}\cos\phi\right)\sum_i m_i^{\text{TM}}\exp(\mathrm{j}kx_i\cos\phi) & \text{TM}\\ \hat{\boldsymbol{z}}\sin\phi\,\text{sinc}^2\left(k\frac{w}{2}\cos\phi\right)\sum_i m_i^{\text{TE}}\exp(\mathrm{j}kx_i\cos\phi) & \text{TE}\end{cases}, \quad (13)$$

where $\boldsymbol{\rho} = \hat{\boldsymbol{x}}x + \hat{\boldsymbol{y}}y$ and $\text{sinc}(x) = \sin(x)/x$.

2.4. PO solutions

Here, we briefly present the PO solutions [29–31, 38] to the aperture problem depicted in figure 1. We do so because the PO approximation is commonly used in Fourier and statistical optics to predict the scattering (or diffraction patterns) from apertures in opaque screens [34, 38]. It is well known that the PO approximation returns inaccurate results for wavelength-scale apertures [29–31]. Later, we show that it also returns inaccurate results for spatially incoherent incident fields, regardless of aperture size.

Returning to equation (4), the PO solution assumes that the aperture field is approximately the incident field, namely,

$$\boldsymbol{\mathcal{M}} \approx \boldsymbol{\mathcal{M}}^{\text{PO}} = -\hat{\boldsymbol{n}}\times E^{\text{inc}}. \quad (14)$$

With this approximate expression for the current, it is simple to derive relations for the TM and TE far-zone electric fields:

$$E^{\text{PO}}(\boldsymbol{\rho}) = \sqrt{\frac{\mathrm{j}k}{2\pi}}\frac{\exp(-\mathrm{j}k\rho)}{\sqrt{\rho}}\begin{cases}-\hat{\boldsymbol{\phi}}\int_{-d/2}^{d/2}E_x^{\text{inc}}(x')\exp(\mathrm{j}kx'\cos\phi)\,\mathrm{d}x' & \text{TM}\\ \hat{\boldsymbol{z}}\sin\phi\int_{-d/2}^{d/2}E_z^{\text{inc}}(x')\exp(\mathrm{j}kx'\cos\phi)\,\mathrm{d}x' & \text{TE}\end{cases}. \quad (15)$$

2.5. CSD functions, SDoCs, and far-zone spectral densities

In this section, we derive relations for the CSD functions and SDoCs of the near-zone MoM and PO fields. These second-order statistical moments show how the near-zone affects the coherence of the scattered field. To examine how these near-field coherence effects impact the far-zone, we also find the MoM and PO far-zone spectral densities (SDs). Although we do find relations for the MoM-based field statistics, these equations are in terms of the impedance matrix $\underline{\mathbf{Z}}$ and therefore, numerical in nature.

Referring back to equation (12), we easily find the currents by

$$\boldsymbol{m} = \underline{\mathbf{Z}}^{-1}\boldsymbol{b}. \tag{16}$$

The CSD function of $\boldsymbol{m}$ is found by multiplying (on the right) both sides of equation (16) by $\boldsymbol{m}^{\dagger}$, where $\dagger$ is the conjugate transpose, and then taking the expectation (ensemble average), namely,

$$\langle \boldsymbol{m}\boldsymbol{m}^{\dagger}\rangle = \underline{\mathbf{W}}_m = \underline{\mathbf{Z}}^{-1}\langle \boldsymbol{b}\boldsymbol{b}^{\dagger}\rangle(\underline{\mathbf{Z}}^{\dagger})^{-1}, \tag{17}$$

where the moment $\langle \boldsymbol{b}\boldsymbol{b}^{\dagger}\rangle$ is the discretized CSD function of the incident field and equal to

$$\langle \boldsymbol{b}\boldsymbol{b}^{\dagger}\rangle = \begin{cases} \frac{4I_0}{k^2}\gamma(x_{j_1} - x_{j_2}) & \text{TM} \\ 4k^2w^2I_0\int_{-1}^{1}\Lambda(t)\gamma[(x_{j_1} - x_{j_2}) - wt]\,\mathrm{d}t & \text{TE} \end{cases}. \tag{18}$$

The SDoC of the currents, which is a direct measure of spatial coherence, is

$$\underline{\boldsymbol{\gamma}}_m = \frac{\underline{\mathbf{W}}_m}{\sqrt{\mathrm{diag}(\underline{\mathbf{W}}_m)[\mathrm{diag}(\underline{\mathbf{W}}_m)]^{\dagger}}}, \tag{19}$$

where $\mathrm{diag}(\underline{\mathbf{X}})$ returns the diagonal elements of $\underline{\mathbf{X}}$ as a vector. The MoM far-zone SD is found by taking the expectation of the magnitude squared of equation (13):

$$\begin{aligned} \langle |E^{\mathrm{MoM}}(\boldsymbol{\rho})|^2\rangle &= S^{\mathrm{MoM}}(\boldsymbol{\rho}) \\ &= \frac{kw^2}{2\pi\rho}\begin{cases} \mathrm{sinc}^2\left(k\frac{w}{2}\cos\phi\right)\sum_{i,j}\langle m_i^{\mathrm{TM}}m_j^{\mathrm{TM}*}\rangle\exp\left[\mathrm{j}k(x_i - x_j)\cos\phi\right] & \text{TM} \\ \sin^2\phi\,\mathrm{sinc}^4\left(k\frac{w}{2}\cos\phi\right)\sum_{i,j}\langle m_i^{\mathrm{TE}}m_j^{\mathrm{TE}*}\rangle\exp\left[\mathrm{j}k(x_i - x_j)\cos\phi\right] & \text{TE}, \end{cases} \end{aligned} \tag{20}$$

where the moments in equation (20) are the TM and TE current CSD functions given in equation (17).

For the PO approximation, the CSD function of the currents is found by taking the autocorrelation of equation (14), which is trivially equal to equation (1); the SDoC of the PO currents is therefore γ. We derive the PO far-zone SD by computing the second moment of equation (15), namely,

$$\begin{aligned} \langle |E^{\mathrm{PO}}(\boldsymbol{\rho})|^2\rangle &= S^{\mathrm{PO}}(\boldsymbol{\rho}) \\ &= \frac{k}{2\pi\rho}\begin{cases} \iint_{-d/2}^{d/2}\langle E_x^{\mathrm{inc}}(x_1')E_x^{\mathrm{inc}*}(x_2')\rangle\exp\left[\mathrm{j}k(x_1' - x_2')\cos\phi\right]\mathrm{d}x_1'\mathrm{d}x_2' & \text{TM} \\ \sin^2\phi\iint_{-d/2}^{d/2}\langle E_z^{\mathrm{inc}}(x_1')E_z^{\mathrm{inc}*}(x_2')\rangle\exp\left[\mathrm{j}k(x_1' - x_2')\cos\phi\right]\mathrm{d}x_1'\mathrm{d}x_2' & \text{TE} \end{cases}. \end{aligned} \tag{21}$$

Substituting in equation (1) and simplifying produces

$$S^{\mathrm{PO}}(\boldsymbol{\rho}) = \frac{kI_0}{2\pi\rho}\int_{-\infty}^{\infty}\left[d^2\mathrm{sinc}^2\left(2\pi\frac{d}{2}t\right)\right]\tilde{\gamma}\left(\frac{k\cos\phi}{2\pi} - t\right)\mathrm{d}t\begin{cases}1 & \text{TM} \\ \sin^2\phi & \text{TE}\end{cases}, \tag{22}$$

where $\tilde{\gamma}$ is the Fourier transform of γ, i.e.,

$$\tilde{\gamma}(f) = \int_{-\infty}^{\infty}\gamma(x)\exp\left(-\mathrm{j}2\pi fx\right)\mathrm{d}x. \tag{23}$$

The bracketed function in the integrand is the Fourier transform of the aperture autocorrelation function $\mathcal{P}$. The far-zone PO SD is therefore proportional to the convolution of the Fourier transforms of $\mathcal{P}$ and γ, and physically is the coherent diffraction pattern filtered or smoothed by $\tilde{\gamma}$ [34, 39, 40].

3. Discussion

Having derived the requisite statistical moments, we now discuss their physical significance. Referring back to equations (17) and (19), we first note that in general, the CSD function and SDoC of the currents—or equivalently, the near field via equation (4)—are not equal to those of the incident field. This stands in contrast

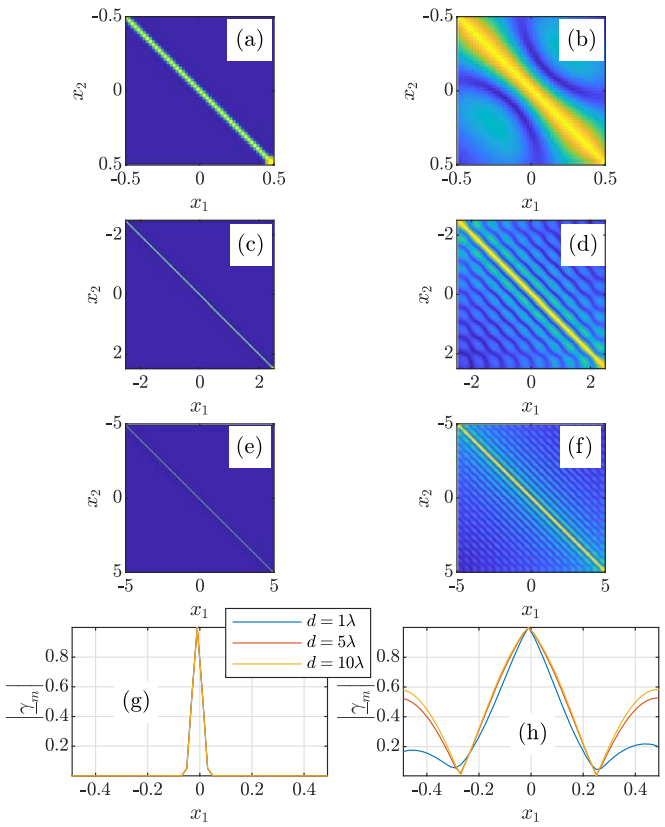

Figure 2. TM and TE SDoC magnitudes with an incoherent incident field (equation (24))—(a) TM $|\underline{\gamma}_m|$ $d = 1\lambda$, (b) TE $|\underline{\gamma}_m|$ $d = 1\lambda$, (c) TM $|\underline{\gamma}_m|$ $d = 5\lambda$, (d) TE $|\underline{\gamma}_m|$ $d = 5\lambda$, (e) TM $|\underline{\gamma}_m|$ $d = 10\lambda$, (f) TE $|\underline{\gamma}_m|$ $d = 10\lambda$, (g) 1D cuts through TM $|\underline{\gamma}_m|$ with $x_2 = 0$, and (h) 1D cuts through TE $|\underline{\gamma}_m|$ with $x_2 = 0$.

to the PO CSD function and SDoC, which are equal to those of the incident field. These statements are true regardless of aperture size.

The fact that the MoM CSD function and SDoC differ from the commonly used PO statistics is not that surprising—even in the absence of surface plasmons. What truly matters is whether these differences give rise to observable effects. To begin addressing this, we start with an approximate, analytically simple model for a spatially incoherent incident field, i.e.,

$$W^{\text{inc}}(x_1, x_2) = I_0 \delta(x_1 - x_2), \tag{24}$$

where $\delta(x)$ is the Dirac delta function [28, 34]. The discretized incident field CSD function $\langle \boldsymbol{b}\boldsymbol{b}^\dagger \rangle$, given in equation (18), is proportional to the identity matrix $\underline{\mathbf{I}}$, and $\underline{\mathbf{W}}_m$ simplifies to

$$\underline{\mathbf{W}}_m \propto (\underline{\mathbf{Z}}^\dagger \underline{\mathbf{Z}})^{-1}. \tag{25}$$

The PO CSD function is equal to equation (24). We note that the incoherent CSD function in equation (24) cannot be represented exactly by the discrete $\langle \boldsymbol{b}\boldsymbol{b}^\dagger \rangle$, which has an equivalent width equal to that of a testing function, or w.

Figure 2 shows the TM and TE SDoC magnitudes corresponding to the discrete CSD function in equation (25) for several values of the aperture width d. The figure is organized into two columns, where the first column shows the TM $|\underline{\gamma}_m|$ and the second column shows the TE $|\underline{\gamma}_m|$. The first 3 rows of figure 2 show the full 2D $|\underline{\gamma}_m|$; row 4 shows the corresponding 1D cuts through $|\underline{\gamma}_m|$ with $x_2 = 0$. To compute $\underline{\mathbf{Z}}$, we discretized the TM and TE aperture currents using $w = \lambda/50$ segments.

It is quite clear from figure 2 that the impact of the near field on coherence is most pronounced in the TE polarization. This is due to the direction of the TE current or aperture field, which is oriented normal to the aperture edge. By visualizing the TE current as numerous tiny magnetic dipole antennas placed end to end, we see physically that this results in significant near-field coupling among 'adjacent' dipoles. Figure 2(h) shows that the widths of the SDoC magnitudes (distances between the first zeros) are $\lambda/2$. We note, however, that there is significant residual coherence for separations beyond $\lambda/2$ extending several λ as seen in figures 2(d) and (f).

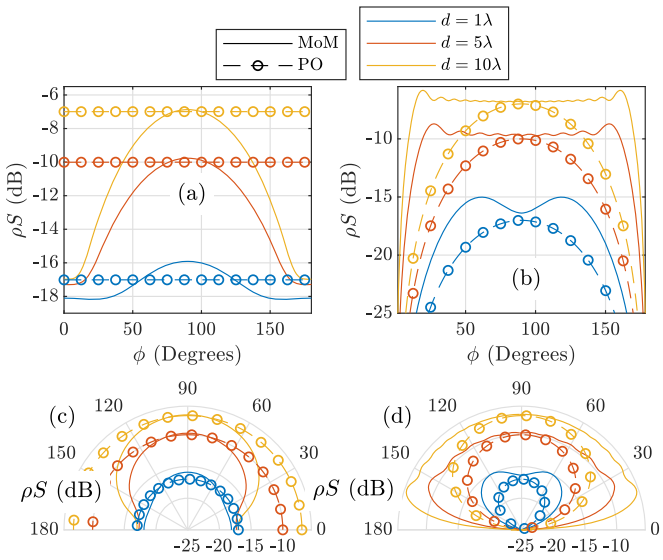

Figure 3. MoM and PO far-zone SDs in dB with an incoherent incident field (equation (24)) and $d = 1\lambda$, 5λ, and 10λ—(a) TM ρS on a Cartesian grid, (b) TE ρS on a Cartesian grid, (c) TM ρS on a polar grid, and (d) TE ρS on a polar grid.

On the other hand, the near zone has little affect on TM fields. The TM current is oriented parallel to the aperture edge in the infinite, or invariant direction. In this case, the tiny magnetic dipole antennas are placed side by side, resulting in negligible coupling between nearby antennas. Figure 2(g) supports this physical picture, showing that the widths of the SDoC magnitudes are approximately $\lambda/10$ and independent of d.

These findings are easily generalized to 3D problems. For instance, assuming a $d_x \times d_y$ rectangular aperture in the x-y plane, the 'TM polarization' scenario applies to the x- and y-directed currents parallel to the aperture edges at $y = \pm d_y/2$ and $x = \pm d_x/2$, respectively. The TE scenario applies to the x- and y-directed currents normal to the aperture edges at $x = \pm d_x/2$ and $y = \pm d_y/2$, respectively. Likewise, for a circular aperture in the x-y plane, the TM and TE scenarios apply to the ϕ- and ρ-directed currents, respectively.

To investigate how the near-field coherence phenomena shown in figure 2 impact the far zone, figure 3 shows the MoM and PO far-zone SDs with an incoherent incident field. Like figures 2, 3 is organized into left and right columns, which show the TM and TE SDs, respectively. Row 1 shows S^{MoM} and S^{PO} on a Cartesian grid; row 2 shows S^{MoM} and S^{PO} on a more physical, polar grid. All SDs are plotted in decibels (dB).

Here, we see differences in the MoM and PO far-zone SDs for both polarizations. Because the PO current CSD function mirrors that of the incident field, S^{PO} is featureless showing no sign of the aperture. In the TE case, it varies with ϕ because of the $\sin^2\phi$ in equation (22). Although S^{MoM} and S^{PO} differ for both polarizations, the differences are much more pronounced in the TE case, especially at large observation angles where we observe directional scattering. We also see partial constructive and destructive interference (ripples) in S^{MoM} in figure 3(b). Since the incident field is incoherent, these telltale signs of (partial) spatial coherence must be due to near-field effects (see figure 2). We do not observe any interference phenomena in S^{PO} or TM S^{MoM}.

Figures 2 and 3 show unequivocally that the near-field most strongly affects coherence in the TE polarization. We therefore focus on the TE case for the remainder of this paper.

We now consider a more realistic incident field CSD function than equation (24), namely,

$$W^{\mathrm{inc}}(x_1, x_2) = I_0 \mathrm{sinc}\left[\frac{k}{\beta}(x_1 - x_2)\right], \tag{26}$$

where $\beta > 0$ is the coherence width (in units of waves) of the incident field. We note that the above CSD function with $\beta = 1$ is consistent with those of blackbody or Lambertian radiators [28], and therefore, could be considered a 'natural' spatially incoherent source.

Figure 4 shows the normalized TE near-field SDs (second moment of the currents), the 1D cuts through the SDoC magnitudes ($x_2 = 0$), and the corresponding S^{MoM} and S^{PO} in dB on polar grids for different β. We assumed $d = 10\lambda$ and discretized the TE current using $w = \lambda/50$ segments.

The results in figure 4 show, not surprisingly, that the PO approximation improves (agrees better with the corresponding MoM result) as β increases, or equivalently, as the incident field becomes more spatially

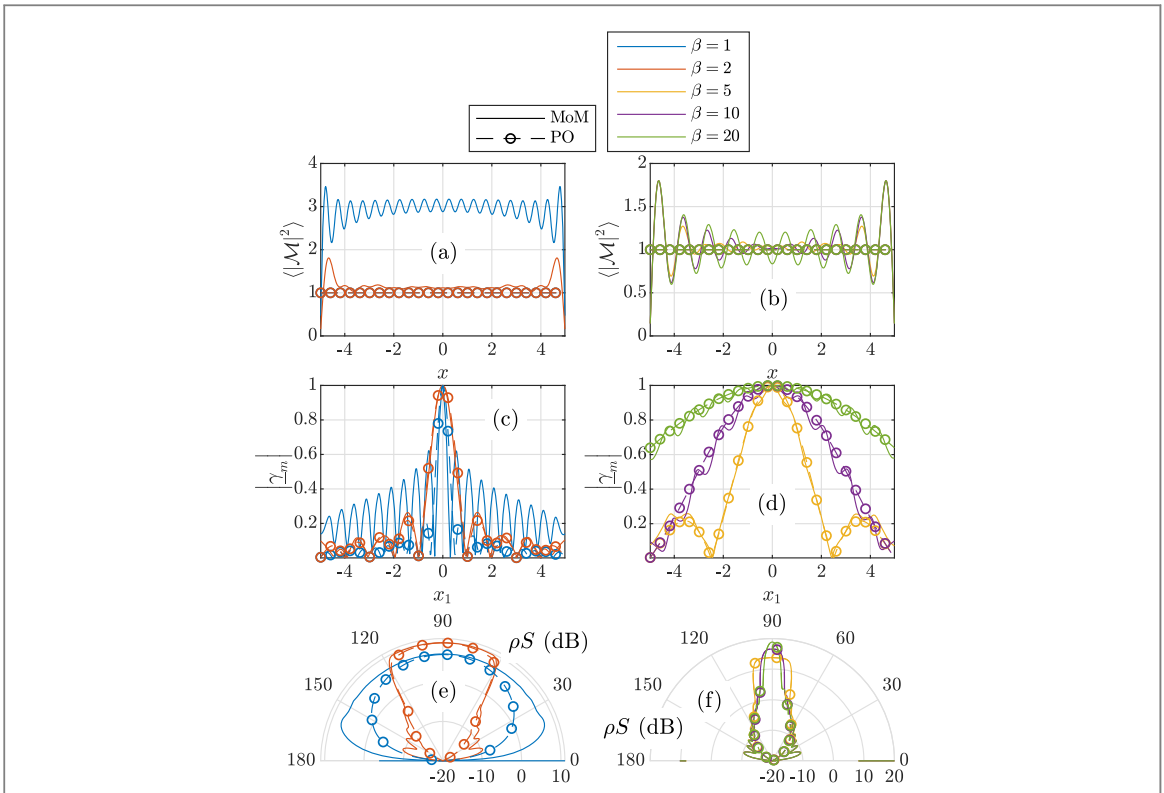

Figure 4. MoM and PO TE near-zone SDs, SDoC magnitudes, and far-zone SDs for $\beta = 1,\ 2,\ 5,\ 10,$ and 20, and $d = 10\lambda$—(a) $\langle|\mathcal{M}|^2\rangle$ for $\beta = 1$ and 2; (b) $\langle|\mathcal{M}|^2\rangle$ for $\beta = 5,\ 10,$ and 20; (c) $|\underline{\gamma}_m|$ with $x_2 = 0$ for $\beta = 1$ and 2; (d) $|\underline{\gamma}_m|$ with $x_2 = 0$ for $\beta = 5,\ 10,$ and 20; (e) ρS in dB on a polar grid for $\beta = 1$ and 2; and (f) ρS in dB on a polar grid for $\beta = 5,\ 10,$ and 20.

coherent. Starting with the current SD results (figures 4(a) and (b)), when $\beta = 1$, the MoM $\langle|\mathcal{M}|^2\rangle$ oscillates with a period equal to $\lambda/2$. The periods of these oscillations lengthen as β increases eventually settling at λ in the coherent limit. With the exception of $\beta = 1$, the MoM $\langle|\mathcal{M}|^2\rangle$ fluctuates around the PO result, which is always unity.

For the SDoC magnitude results (figures 4(c) and (d)), there is good agreement between the MoM and PO $|\underline{\gamma}_m|$ except when $\beta = 1$, which is the most interesting case. While the width of the $\beta = 1$ MoM $|\underline{\gamma}_m|$ is approximately equal to the PO SDoC magnitude (a sinc(x) function, see equation (26)), the 'side lobes' are significantly higher for the MoM $|\underline{\gamma}_m|$. This physically means that the scattered field is spatially more coherent than predicted by the commonly used PO approximation.

Lastly, figures 4(e) and (f) show the far-zone SD results, where, again, we observe significant differences between S^{MoM} and S^{PO} when $\beta = 1$. Like the SD results in figure 3, these differences are most noticeable at large scattering angles.

We note here that $d = 10\lambda$, which is large enough for the PO approximation to be accurate (see the $\beta = 20$ results in figure 4(f)). The $\beta = 1$ results in figure 4 show that the PO approximation gives nonphysical results for incoherent incident fields. This finding is independent of aperture size and a key result in this paper.

4. Young's experiment

In the previous section, we showed and explained that because of the direction of the TE current, significant near-field coupling occurs, generally resulting in an increase in spatial coherence. Here, we investigate this phenomenon further using a two-slit geometry, i.e., Thomas Young's experiment [28, 34]. The purpose is to observe interference of the light emitted from the two slits when illuminated by a spatially incoherent TE field. The two-slit geometry is similar to that depicted in figure 1—the difference being that there are now two apertures (of width d) centered on the origin and spaced D apart (when measured from center to center).

The MoM CSD and SDoC are still, in general, given by equations (17) and (19); however, the TE MFIE is now a system of coupled MFIEs in terms of the currents in slits 1 and 2:

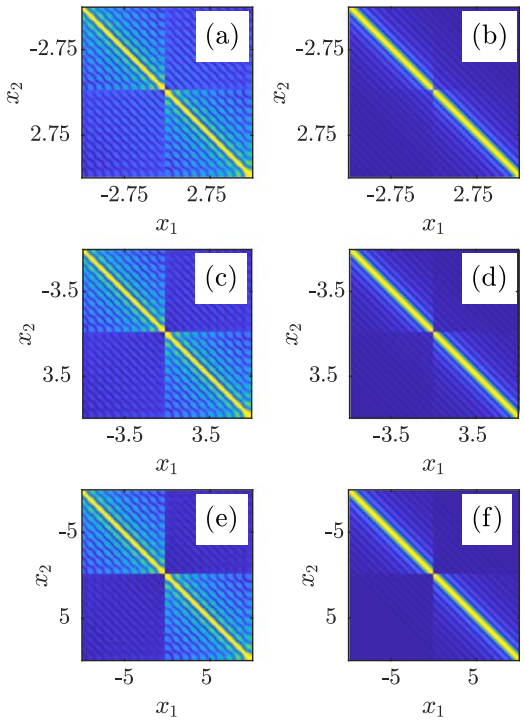

Figure 5. MoM and PO SDoC magnitudes for an incident field CSD function given by equation (26) with $\beta = 1$ and $D = 1.1d = 5.5\lambda$, $1.4d = 7\lambda$, and $2d = 10\lambda$—(a) MoM $|\underline{\gamma}_m|$ $D = 5.5\lambda$, (b) PO $|\underline{\gamma}_m|$ $D = 5.5\lambda$, (c) MoM $|\underline{\gamma}_m|$ $D = 7\lambda$, (d) PO $|\underline{\gamma}_m|$ $D = 7\lambda$, (e) MoM $|\underline{\gamma}_m|$ $D = 10\lambda$, and (f) PO $|\underline{\gamma}_m|$ $D = 10\lambda$.

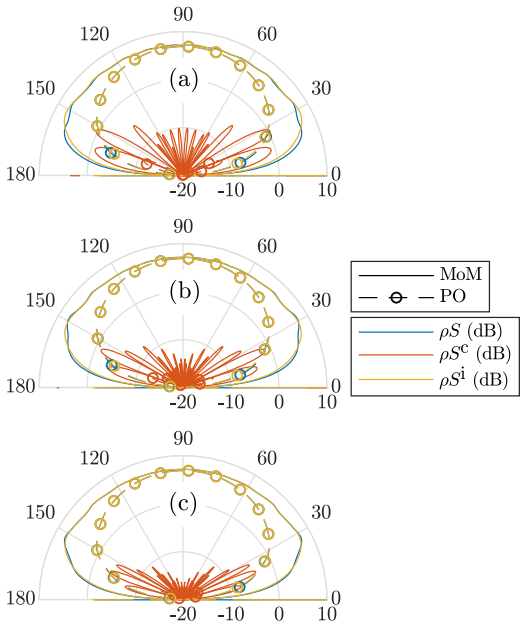

Figure 6. MoM and PO far-zone full, coherent, and incoherent SDs for an incident field CSD function given by equation (26) with $\beta = 1$ and $D = 1.1d = 5.5\lambda$, $1.4d = 7\lambda$, and $2d = 10\lambda$—(a) $D = 5.5\lambda$, (b) $D = 7\lambda$, and (c) $D = 10\lambda$.

$$2kE_z^{\text{inc}}(x) = \left(k^2 + \frac{\partial^2}{\partial x^2}\right)\sum_{n=1}^{2}\int_{S_n} \mathcal{M}_n^{\text{TE}}(x')H_0^{(2)}(k|x - x'|)\,\mathrm{d}x' \quad x \in S_1$$
$$2kE_z^{\text{inc}}(x) = \left(k^2 + \frac{\partial^2}{\partial x^2}\right)\sum_{n=1}^{2}\int_{S_n} \mathcal{M}_n^{\text{TE}}(x')H_0^{(2)}(k|x - x'|)\,\mathrm{d}x' \quad x \in S_2, \tag{27}$$

where $S_1 = [-D/2 - d/2, -D/2 + d/2]$ and $S_2 = [D/2 - d/2, D/2 + d/2]$. The same triangular basis and rectangular testing functions that were used in the single aperture problem are used here as well. Since the analysis is very similar to that presented in section 2.3, we omit the details for the sake of brevity. The MoM far-

zone SD is easily found by generalizing equation (13) and becomes

$$\begin{aligned} S^{\mathrm{MoM}}(\boldsymbol{\rho}) &= S^{\mathrm{MoM,i}}(\boldsymbol{\rho}) + S^{\mathrm{MoM,c}}(\boldsymbol{\rho}) \\ S^{\mathrm{MoM,i}}(\boldsymbol{\rho}) &= \frac{kw^2}{2\pi\rho}\sin^2\phi\,\mathrm{sinc}^4\left(k\frac{w}{2}\cos\phi\right) \\ &\quad\times\left[\sum_{i_1,i_2}\langle m_{1i_1}^{\mathrm{TE}} m_{1i_2}^{\mathrm{TE}*}\rangle\exp\left[\mathrm{j}k(x_{i_1}-x_{i_2})\cos\phi\right] + \sum_{j_1,j_2}\langle m_{2j_1}^{\mathrm{TE}} m_{2j_2}^{\mathrm{TE}*}\rangle\exp\left[\mathrm{j}k(x_{j_1}-x_{j_2})\cos\phi\right]\right] \\ S^{\mathrm{MoM,c}}(\boldsymbol{\rho}) &= \frac{kw^2}{2\pi\rho}\sin^2\phi\,\mathrm{sinc}^4\left(k\frac{w}{2}\cos\phi\right) \\ &\quad\times\left[\sum_{i_1,j_2}\langle m_{1i_1}^{\mathrm{TE}} m_{2j_2}^{\mathrm{TE}*}\rangle\exp\left[\mathrm{j}k(x_{i_1}-x_{j_2})\cos\phi\right] + \sum_{j_1,i_2}\langle m_{2j_1}^{\mathrm{TE}} m_{1i_2}^{\mathrm{TE}*}\rangle\exp\left[\mathrm{j}k(x_{j_1}-x_{i_2})\cos\phi\right]\right], \end{aligned} \tag{28}$$

where the superscripts 'i' and 'c' stand for incoherent and coherent, respectively. The incoherent contribution to the SD $S^{\mathrm{MoM,i}}$ contains the self terms, i.e., contains the autocorrelations of the currents in slits 1 and 2. The coherent contribution $S^{\mathrm{MoM,c}}$ contains the coupling terms, viz., the cross correlations of the currents in slits 1 and 2. The magnitudes of these cross correlations (they are equal) determine to what extent the light emitted from one slit interferes with the light emitted from the other.

The PO CSD and SDoC mirror those of the incident field. Like the MoM far-zone SD, S^{PO} is easily derived by generalizing equation (22), namely,

$$S^{\mathrm{PO}}(\boldsymbol{\rho}) = \frac{kI_0}{2\pi\rho}\sin^2\phi\int_{-\infty}^{\infty} d^2\mathrm{sinc}^2\left(2\pi\frac{d}{2}t\right)[2+2\cos(2\pi Dt)]\tilde{\gamma}\left(\frac{k\cos\phi}{2\pi}-t\right)\mathrm{d}t. \tag{29}$$

The incoherent and coherent terms of S^{PO} are

$$\begin{aligned} S^{\mathrm{PO,i}}(\boldsymbol{\rho}) &= 2\frac{kI_0}{2\pi\rho}\sin^2\phi\int_{-\infty}^{\infty} d^2\mathrm{sinc}^2\left(2\pi\frac{d}{2}t\right)\tilde{\gamma}\left(\frac{k\cos\phi}{2\pi}-t\right)\mathrm{d}t \\ S^{\mathrm{PO,c}}(\boldsymbol{\rho}) &= 2\frac{kI_0}{2\pi\rho}\sin^2\phi\int_{-\infty}^{\infty} d^2\mathrm{sinc}^2\left(2\pi\frac{d}{2}t\right)\cos(2\pi Dt)\tilde{\gamma}\left(\frac{k\cos\phi}{2\pi}-t\right)\mathrm{d}t. \end{aligned} \tag{30}$$

Figure 5 shows the full 2D MoM and PO SDoC magnitudes for several values of D. The first column of images in figure 5 shows the MoM $|\underline{\gamma}_m|$; the second column shows the PO SDoC magnitudes. The x and y tick marks (∓ 2.75, ∓ 3.5, and ∓ 5) demark the centers of slits 1 and 2, respectively. Figure 6 shows the corresponding S^{MoM} and S^{PO}, plus their incoherent and coherent contributions. Here, we assumed the slits were $d = 5\lambda$, the currents were discretized using $w = \lambda/50$ segments, and the incident field CSD function was given by equation (26) with $\beta = 1$.

The SDoC magnitudes in figure 5 are block 2×2, with the off-diagonal blocks physically showing how much one slit coherently couples to the other. As physically expected, the amplitudes of these blocks decrease as D increases. In addition, one notices that the off-diagonal block amplitudes for the MoM $|\underline{\gamma}_m|$ are significantly higher than the corresponding PO SDoC magnitudes, which are very weak. This means that, although illuminated by a spatially incoherent field, the light emitted from the two slits is actually partially coherent, and near-field physics are responsible for the transformation.

Figure 6 shows the extent to which coherent near-field coupling is observable in the far zone. For all values of D, there is a coherent contribution to S^{MoM} which causes observable (in some cases, minor) differences between S^{MoM} and $S^{\mathrm{MoM,i}}$ located predominately at large scattering angles. As physically expected, these differences are most noticeable when D is the smallest (see figure 6(a)). We observe no discernible differences between S^{PO} and $S^{\mathrm{PO,i}}$.

5. Conclusion

In this paper, we studied how the near field affects spatial coherence considering phenomena other than surface plasmons, whose role is well documented. We derived the second-order statistical moments of the field (CSD functions, SDoCs, and far-zone SDs) scattered from an aperture in an infinite PEC screen (a structure that does not support surface plasmons) using both rigorous EM theory and the commonly used PO approximation. We compared and contrasted the EM and PO field statistics and discussed their physical significance at length.

From our analysis, we concluded that the near field does impact spatial coherence, even in the absence of surface plasmons, and the effects are observable. By examining the far-zone SDs and assuming a spatially incoherent incident field, we found that near-field coherence effects were most noticeable at large, nonparaxial

scattering angles, where significant differences were noted between the EM and PO SDs. Most interestingly, we found that this held true even for optically (or electrically) large apertures, where PO was assumed to be accurate.

To further examine these effects, we considered the near- and far-zone field statistics of Young's classic, two-slit experiment. Even with an incoherent incident field and large, widely separated apertures, we observed interference of the light emitted from the slits implying that near-field physics had increased the spatial coherence of the field.

The analysis and findings presented in this work complement the prior theoretical and experimental coherence research involving surface plasmons, and could find use in future, compact, low-power devices designed to manipulate or control spatial coherence.

Acknowledgments

The views expressed in this paper are those of the authors and do not reflect the official policy or position of the US Air Force, the Department of Defense, or the US government.

ORCID iDs

Milo W Hyde IV https://orcid.org/0000-0003-2814-202X

References

[1] Hesketh P J, Zemel J N and Gebhart B 1988 *Phys. Rev.* B **37** 10795–802
[2] Hesketh P J, Zemel J N and Gebhart B 1988 *Phys. Rev.* B **37** 10803–13
[3] Carminati R and Greffet J J 1999 *Phys. Rev. Lett.* **82** 1660–3
[4] Henkel C, Joulain K, Carminati R and Greffet J J 2000 *Opt. Commun.* **186** 57–67
[5] Marquier F, Joulain K, Mulet J P, Carminati R, Greffet J J and Chen Y 2004 *Phys. Rev.* B **69** 155412
[6] Greffet J J, Carminati R, Joulain K, Mulet J P, Mainguy S and Chen Y 2002 *Nature* **416** 61–4
[7] Sai H and Kanamori Y 2003 *Microscale Thermophys. Eng.* **7** 101–15
[8] Lee B J, Fu C J and Zhang Z M 2005 *Appl. Phys. Lett.* **87** 071904
[9] Laroche M, Carminati R and Greffet J J 2006 *Phys. Rev. Lett.* **96** 123903
[10] Wadsworth S L, Clem P G, Branson E D and Boreman G D 2011 *Opt. Mater. Express* **1** 466–79
[11] Gan C H, Gbur G and Visser T D 2007 *Phys. Rev. Lett.* **98** 043908
[12] Kuzmin N, 't Hooft G W, Eliel E R, Gbur G, Schouten H F and Visser T D 2007 *Opt. Lett.* **32** 445–7
[13] Gan C H, Gu Y, Visser T D and Gbur G 2012 *Plasmonics* **7** 313–22
[14] Saastamoinen T and Lajunen H 2013 *Opt. Lett.* **38** 5000–3
[15] Divitt S, Frimmer M, Visser T D and Novotny L 2016 *Opt. Lett.* **41** 3094–7
[16] Norrman A, Ponomarenko S A and Friberg A T 2016 *Europhys. Lett.* **116** 64001
[17] Li D and Pacifici D 2017 Strong amplitude and phase modulation of optical spatial coherence with surface plasmon polaritons *Sci. Adv.* **3** e1700133 http://advances.sciencemag.org/content/3/10/e1700133
[18] Korotkova O 2014 *Random Light Beams: Theory and Applications* (Boca Raton, FL: CRC)
[19] Cai Y, Chen Y, Yu J, Liu X and Liu L 2017 *Prog. Opt.* **62** 157–223
[20] Hyde M W, Bose-Pillai S, Voelz D G and Xiao X 2016 *Phys. Rev. Applied* **6** 064030
[21] Hyde M W IV, Bose-Pillai S, Xiao X and Voelz D G 2017 *J. Opt.* **19** 025601
[22] Visser T D, Agrawal G P and Milonni P W 2017 *Opt. Lett.* **42** 4600–2
[23] Hyde M W, Basu S, Voelz D G and Xiao X 2015 *J. Appl. Phys.* **118** 093102
[24] Maier S A and Andrews S R 2006 *Appl. Phys. Lett.* **88** 251120
[25] Pendry J B, Martín-Moreno L and Garcia-Vidal F J 2004 *Science* **305** 847–8
[26] Maradudin A A 2014 Surface electromagnetic waves on structured perfectly conducting surfaces *Modern Plasmonics* (*Handbook of Surface Science* Vol 4) ed N Richardson and S Holloway (Amsterdam, The Netherlands: Elsevier) Ch 7, pp 223–251
[27] Huidobro P, Fernández-Domínguez A I, Pendry J B, Martín-Moreno L and Garcia-Vidal F 2018 *Spoof Surface Plasmon Metamaterials Elements* (*Emerging Theories and Technologies in Metamaterials*) (Cambridge, UK: Cambridge)
[28] Mandel L and Wolf E 1995 *Optical Coherence and Quantum Optics* (New York, NY: Cambridge University)
[29] Balanis C A 2012 *Advanced Engineering Electromagnetics* 2nd edn (Hoboken, NJ: Wiley)
[30] Jin J M 2015 *Theory and Computation of Electromagnetic Fields* 2nd edn (Hoboken, NJ: Wiley)
[31] Harrington R F 2001 *Time-Harmonic Electromagnetic Fields* (New York, NY: IEEE)
[32] Harrington R F 1993 *Field Computation by Moment Methods* (Piscataway, NJ: IEEE)
[33] Peterson A F, Ray S L and Mittra R 1998 *Computational Methods for Electromagnetics* (Piscataway, NJ: IEEE)
[34] Goodman J W 2015 *Statistical Optics* 2nd edn (Hoboken, NJ: Wiley)
[35] Mittra R, Hall R and Tsao C H 1984 *IEEE Trans. Antennas Propag.* **32** 533–6
[36] Frenkel A 1989 *IEEE Trans. Antennas Propag.* **37** 1211–4
[37] Gibson W C 2014 *The Method of Moments in Electromagnetics* 2nd edn (Boca Raton, FL: CRC)
[38] Goodman J W 2005 *Introduction to Fourier Optics* 3rd edn (Englewood, CO: Roberts & Company)
[39] Schell A 1967 *IEEE Trans. Antennas Propag.* **15** 187–8
[40] Shore R A, Thompson B J and Whitney R E 1966 *J. Opt. Soc. Am.* **56** 733–8